Highlights

Aeroacoustic noise prediction of ducted wind turbine rotor

Rui Pedro Gonçalves, Sophie Le Bras, J. Manoel Freire-Guimaraes, Christophe Schram

- Ducted Rotor's broadband trailing edge noise prediction using Amiet theory, predicting peak noise level and frequency within 4 dB accuracy.
- Prediction of BPFH rotor's tonal loading noise in free field.
- Diffuser's influence on the scattering of the tonal loading noise using Finite Element Method.

Aeroacoustic noise prediction of ducted wind turbine rotor

Rui Pedro Gonçalves[a,b,*], Sophie Le Bras[c], J. Manoel Freire-Guimaraes[d], Christophe Schram[a]

[a] *von Karman Institute for Fluid Dynamics, 72 chaussée de Waterloo, St-Genesius-Rode, 1640, Belgium*
[b] *University of Twente, PO Box 217, Enschede, 7500 AE, The Netherlands*
[c] *Siemens Industry Software SAS, 107 avenue de la République, Châtillon, 92320, France*
[d] *Delft University of Technology, Delft, The Netherlands*

Abstract

Wind turbines coupled with a diffuser-augmented configuration have demonstrated potential to significantly enhance energy extraction. Their compact size proves to be ideal for urban wind energy harvesting. However, the presence of these devices in urban areas raises concerns regarding noise emissions. In this study, a simulation workflow is designed to predict the rotor aerodynamic noise of diffuser-augmented wind turbines, with focus on the rotor's dominant sound sources, broadband trailing edge noise and tonal noise. Two hybrid approaches were implemented, solving the flow with either a 3D RANS or 2D strip approach, and coupling with aeroacoustic analytical models for noise prediction. For the aeroacoustic analysis, Amiet theory was used for the computation of the trailing edge broadband noise. As for the tonal noise prediction, finite element method was used to predict the steady loading tonal noise component, and the scattering effect caused by the presence of the diffuser. We find the adopted low order methodology is capable of predicting the broadband noise spectrum peak levels and frequencies with an accuracy of around 4 dB for both considered approaches. As for the tonal noise, we show how the diffuser scatters the tonal noise produced by the first harmonic blade passing frequency.

*Corresponding author
Email address: rui.goncalves@vki.ac.be (Rui Pedro Gonçalves)
[1] PhD candidate, Environmental and Applied Fluid Dynamics dept, von Karman Institute for Fluid Dynamics

Keywords: Ducted wind turbine, Urban Wind Energy, Aeroacoustics

1. Introduction

As cities expand and energy demands surge, the need for sustainable and efficient energy sources intensifies. This is particularly crucial given the increasing population densities in urban areas and rising domestic energy usage, encouraging discussions about optimal energy sources and ideal placement (Mahmood et al., 2021). Furthermore, the demand for carbon neutrality forces us to seek renewable energy sources. The transition is already underway, with many European countries consuming more than half of their energy from renewable sources, including wind, hydro, biomass, and solar.

Harvesting wind energy in an urban environment poses challenges, such as maintaining high energy yields, or the inconvenience caused by the visual and noise pollution. As urban areas regulate a maximum noise limit, the noise emissions must be predicted and projected at a design phase, under the penalty of impeding the installation of the device. Both aerodynamic and the aeroacoustic aspects must therefore be considered when planning for a viable installation of wind turbines in urban areas.

The diffuser-augmented wind turbine (DAWT) is a compact solution suited for the urban environment conditions, characterized by frequent direction changes. It can be installed either on the street or mounted on the roof or facade of buildings, as illustrated in Fig. 1. Despite not as flexible with wind directions as vertical axis wind turbines, DAWT provide an higher power coefficient (C_P), a metric of wind turbine efficiency.

Figure 1: Building mounted Diffuser-Augmented Wind Turbine - © [erikdegraaf] / Adobe Stock

As depicted in Fig. 2, a DAWT is characterized by its ducted structure, specifically designed with a diffuser shape. Unlike traditional wind turbines, the DAWT employs a casing with a divergent outlet, often airfoil shaped. A proper design of the diffuser reduces the static pressure downstream of the rotor, leading to an increase in mass flow across the rotor plane, which enhances the turbine power extraction potential, as explained in Hansen et al. (2000).

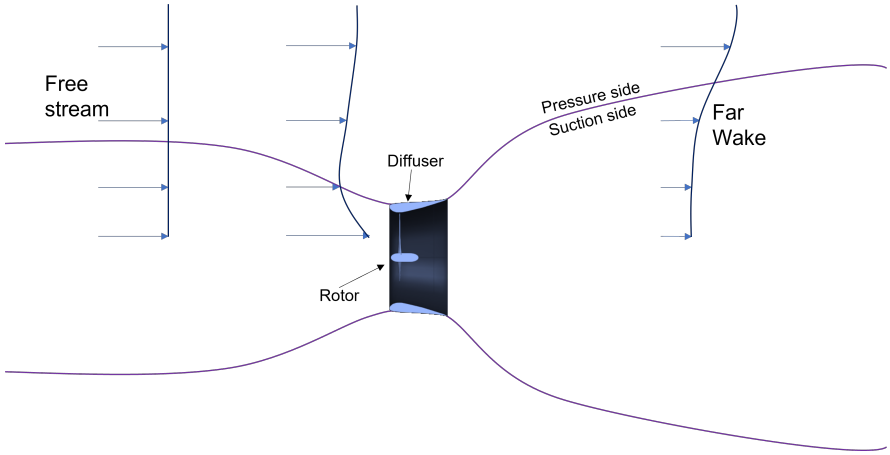

Figure 2: Schematic of Diffuser-Augmented Wind Turbine and evolution of axial velocity profiles.

This effect allows capturing airflow from a greater inflow area with the same rotor dimension resulting in higher flow velocities crossing the rotor plane, and an increase of the C_P with respect to the bare rotor. This metric quantifies the wind turbine efficiency, as the ratio of the power extracted P_T to the total available wind energy potential, based on the rotor area and wind speed (Lanzafame and Messina, 2010):

$$C_P = \frac{P_T}{\frac{1}{2}\rho\, A_{\text{rotor}}\, U_{\text{wind}}^3} \tag{1}$$

where ρ is the air density, A_{rotor} the rotor sweeping area and U_{wind} is the mean wind inflow velocity.

The aerodynamic noise of DAWTs features several dominant sources (Fig. 3), with distinct frequency ranges and intensities. The rotor mainly con-

tributes with broadband trailing edge (TE) noise and, when incoming turbulence is present, broadband leading edge (LE) noise as well. The rotor tonal noise typically occurs at the first few multiples of the blade passing frequency (BPF), and may have considerable amplitude at the first BPF. In addition, the diffuser produces broadband trailing edge noise and scatters the rotor noise.

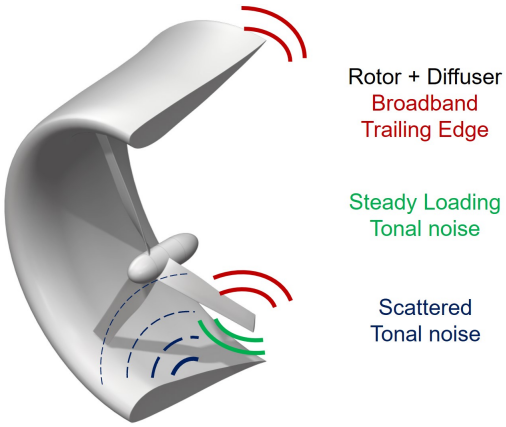

Figure 3: Rotor tonal, TE and LE broadband noise and diffuser TE broadband noise are the dominant noise sources.

Aerodynamic performance can be predicted using low-order approaches such as axial momentum theory (MT) or blade element momentum theory (BEMT) models (Bontempo and Manna, 2017). In these approaches, the wind turbine rotor is modelled as an actuator disk, modelling the exchange of momentum between the rotor blades and the flow as a uniformly distributed pressure drop. To model the induction of the diffuser, the actuator disk can be combined with panel methods (Bontempo and Manna, 2020), assuming that viscous effects are of secondary importance. Increasing the accuracy and computational costs, Reynolds-averaged Navier-Stokes (RANS) CFD solvers can be used to resolve the flow around the blades, accounting for the development of the boundary layers along the diffuser (Leloudas et al., 2020; Bontempo et al., 2023). On the high-fidelity side, scale-resolved CFD methods as in Avallone et al. (2020), provide a detailed description of the spatio-temporal features of the turbulent flow.

On the acoustic side as well, a range of simulation techniques are available, by increasing order of accuracy and numerical cost: empirical tools calibrated

on experimental databases (Brooks et al., 1989), analytical models, semi-analytical methods, incompressible transient CFD-based hybrid methods or Direct Noise Computations (DNC).

The analytical, semi-analytical models and hybrid transient CFD-based approaches are mostly based on the aeroacoustic analogies established by Curle (1955) and Ffowcs Williams and Hawkings (1969). Analytical models can predict rotor tonal noise based on blade thickness and steady loading (Hanson, 1980; Roger, 2007). The semi-analytical methods assume canonical interactions between turbulence and thin airfoils to predict broadband noise in a statistical sense (Amiet, 1975, 1976; Bresciani et al., 2022), the turbulence statistics being typically obtained from RANS simulations. The hybrid CFD-based approach uses time-resolved simulations of the flow field, from which equivalent sources are calculated, the sound propagation being handled by a suitable Green's function (Ghasemian and Nejat, 2015; Weber et al., 2015; Kaltenbacher et al., 2017; Cabrol et al., 2012; Piellard and Bailly, 2008). In contrast, in the DNC approach, the compressible Navier-Stokes equations (Zhu et al., 2018) or Boltzmann equations (Dighe et al., 2020) are directly solved using low-dissipative and low-dispersive discretization schemes, providing both the aerodynamic and acoustic fields without resorting to an acoustic analogy. The numerical costs associated with the latter renders them however impractical for engineering design and optimization purposes. Regarding the accuracy, noise predictions within 2 dB Oerlemans and Schepers (2009) or up to 3 dB Bresciani et al. (2022) is considered satisfactory when compared to measurements for large wind turbines. Similar accuracy was deemed acceptable for noise prediction of smaller urban wind turbinesBrandetti et al. (2023).

The objective of this paper is to expand upon existing DAWTs noise prediction methodologies and to propose low-CPU alternatives combining steady RANS and inviscid simulations with analytical and semi-analytical methods to predict the tonal and broadband noise emitted by the rotor blades, accounting for the induction effect of the diffuser. The main question that is tackled here is to which extent the three-dimensional and viscous effects can be simplified or neglected while maintaining a meaningful acoustic prediction.

The paper is organized as follows: Section 2 describes the numerical methodologies used in the present study, describing both aerodynamic and aeroacoustic models. The aerodynamic and aeroacoustic results are then presented in Section 3. Finally, Section 4 provides conclusions.

2. Methods

In this work, the focus is put on the broadband and tonal noise emitted by the DAWT rotor, discarding the diffuser self noise. For the tonal noise predictions, we also account for the sound scattering effects by the diffuser.

The simulation workflow developed in this study is illustrated in Fig. 4. It is composed of flow prediction models combined with aeroacoustics models which are presented in this section. This workflow is applied to a DAWT case which is briefly described in the following.

2.1. Duct-augmented Wind turbine

The turbine used in this study is the DonQi DAWT, designed by Nederlands Lucht-en Ruimtevaartcentrum (NLR) and optimized in later studies (Hoopen, 2009; Van and Eng, 2011). The ducted turbine is shown in Fig. 5 and its main parameters are provided in Tab. 1. The design includes a rotor made of three equally spaced blades. The rotor has a radius of 0.75 m, and the blades are shaped with the NACA-2207 profile. The rotor is placed at the throat of a convergent-divergent diffuser, with a tip clearance of 2.5 % of the radial distance, and the radial distributions for blade chord and twist were sourced from Avallone et al. (2020). The blade pitch angle is of 10°, and is included in the CAD model.

The streamwise length of the diffuser is equal to 1 m. The diffuser has a diameter of 1.74 m at its leading edge and 2 m at its trailing edge, giving an opening angle based on those two points equal to 11°.

The rotation speed is equal to 380 RPM, and the incoming flow has a velocity of $5\,\mathrm{m\,s^{-1}}$ aligned with the rotation axis, matching conditions already reported in the literature by Anselmi (2017); Avallone et al. (2020); Küçükosman (2019).

Table 1: DonQi turbine parameters and operating conditions (Avallone et al., 2020).

Chord length c, at blade hub	0.13 m
Chord length c, at blade tip	0.105 m
Blade tip radius r	0.75 m
Freestream velocity $U*_\infty$	$5\,\mathrm{m\,s^{-1}}$
Rotational speed Ω	380 RPM
Thrust Coefficient C_T	0.865
Blade pitch	10°

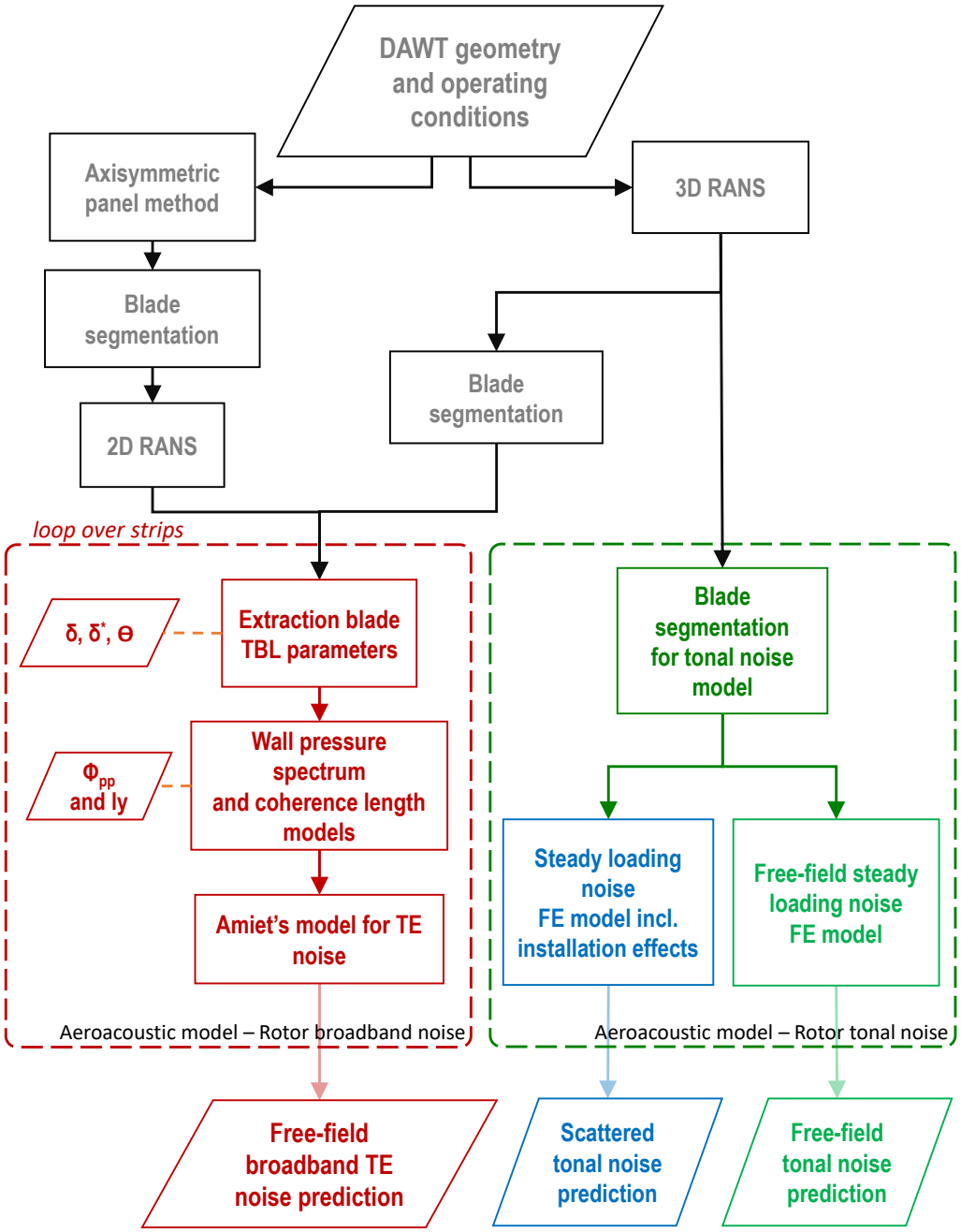

Figure 4: Simulation flowchart.

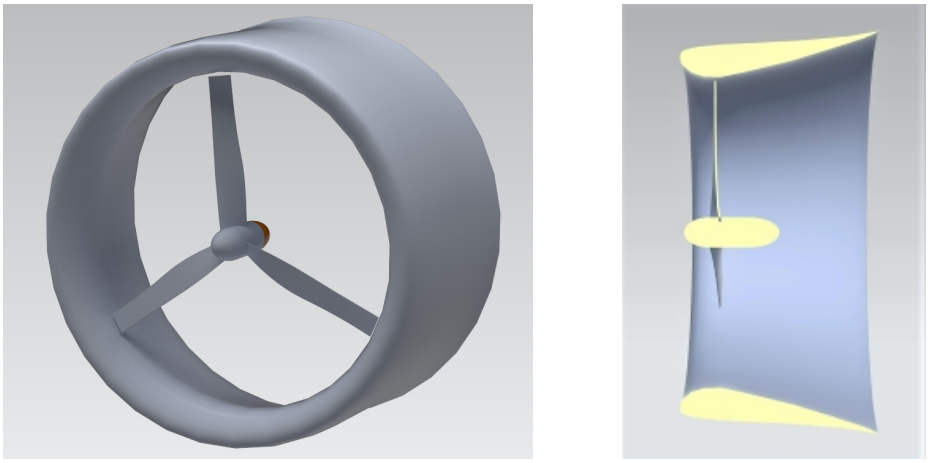

Figure 5: 3D CAD and section cut view of the DonQi DAWT.

2.2. Aeroacoustic model

The noise source mechanisms considered in this work are the steady loading tonal noise and the broadband noise resulting from the interaction of the blades boundary layers with their trailing-edge (TE).

2.2.1. Tonal steady-loading noise in free field and scattered by the diffuser

The formalism offered by Ffowcs Williams and Hawkings (1969) has been followed to predict the tonal noise emissions. Given the low tip Mach number ($M_{\text{tip}} = 0.09$) and the acoustic compactness of the blades for the first Blade Passing Frequencies (19 Hz, 38 Hz, ...), the contribution of the quadrupolar noise has been omitted (Roger, 2019). Also, we neglect the monopole source term related to volume displacement, which would become significant for larger Mach numbers as well (Hanson, 1980).

The tonal loading noise emitted by one blade can be either represented as a rotating dipole, or as an array of fixed and phase-shifted dipoles. Both formulations are valid in the acoustic and geometrical near-field. The latter formulation presents the advantage of supporting propagation in non-homogeneous media when coupled with finite element method. Such fixed dipole approach, implemented in commercial software Simcenter 3D Acoustics(Siemens Digital Industries Software, 2022a; Kucukcoskun and Kierkegaard, 2022), is used in this work.

Simcenter 3D Acoustics features an adaptive order finite-element formulation (FEMAO), proposed by Bériot et al. (2016), for the resolution of the

Helmholtz equation. The FEMAO approach relies on a high-order continuous Galerkin finite element method equipped with a basis of Legendre polynomials. Bériot et al. (2016) have shown that FEMAO provides substantial reductions in memory and CPU costs compared to standard low-order FEM approaches for acoustics. The polynomial order in each FEM element is automatically selected for each frequency of interest using an a priori indicator, enabling the use of a single coarse mesh and thereby optimizing the computational efficiency for broad frequency studies (Bériot et al., 2016; Gabard et al., 2018). For computational efficiency, the FEM domain can be restricted to a small region surrounding the DAWT. In order to minimize spurious noise reflections at the external boundaries of the FEM domain, an Automatically Matched Layer (AML) is used, as explained in Bériot and Modave (2021). The sound levels can be computed at far-field microphones located out the FEM domain thanks to a Kirchhoff sound extrapolation.

The numerical implementation of the fixed dipole array formulation involves as a first step the surface integration of the pressure field obtained from the incompressible CFD solution, over compact blade segments. In order to ensure the compactness of the dipole sources, the blade segment length, denoted L_s is defined as a function of the speed of sound c_0 and the maximum frequency of interest $f_{\max}$ for the noise predictions as:

$$L_s = \frac{c_0}{N_s f_{\max}} \tag{2}$$

where $N_s = 4$ is the number of segments per acoustic wavelength.

In order to mimic the propeller rotation, the rotation of the dipoles is discretized. At each position around the rotation axis, the dipole strength is mapped onto the local Degrees of Freedom (DoFs) of the high order FEM element on the dipole's trajectory. For each high order DoF, a sound source term is thus obtained and used as a right-hand side term in the FEM problem.

In free-field, the FEM results have been compared with the solution provided by Roger (2007):

$$p(\mathbf{x}, \omega) = \frac{\mathrm{i}k}{4\pi} \frac{1}{T} \int_0^T \frac{\mathbf{F} \cdot \mathbf{R}}{R^2} \left(1 + \frac{1}{\mathrm{i}kR}\right) \mathrm{e}^{-\mathrm{i}\omega\,(\tau + R/c_0)}\, \mathrm{d}\tau \tag{3}$$

where $k = \omega / c_0$ is the acoustic wavenumber based on the sound speed c_0, and T is the period of integration of the Fourier transform (usually a couple of rotation periods to ensure convergence). The rotating force vector $\mathbf{F}$ is

defined by its axial (thrust), tangential (drag) and radial components F_T, F_D and F_R, respectively, expressed in a rotating reference frame attached to the blade:

$$\mathbf{F} = (-F_D \sin\gamma + F_R \cos\gamma, F_D \cos\gamma + F_R \sin\gamma, -F_T) \ .$$

with $\gamma = \Omega t$. $\mathbf{R}$ is the vector from the point dipole to the listener, given by:

$$\mathbf{R} = (x \sin\theta \cos\varphi - r' \cos\gamma, x \sin\theta \sin\varphi - r' \sin\gamma, x \cos\theta)$$

taking the center of the rotor as origin. The validation of the Simcenter3D Acoustics numerical implementation with a Matlab discretization of (3) is provided in Section 3.

Another benefit of the FEM approach is that it can account for acoustic scattering effect by arbitrary geometries. In this work, we will focus on the acoustic scattering by the diffuser which is included in the FEM domain. In this approach the rotor dipoles are centered in the fluid domain, and the diffuser solid body is modelled by absence of acoustic fluid mesh, as illustrated in Fig. 6.

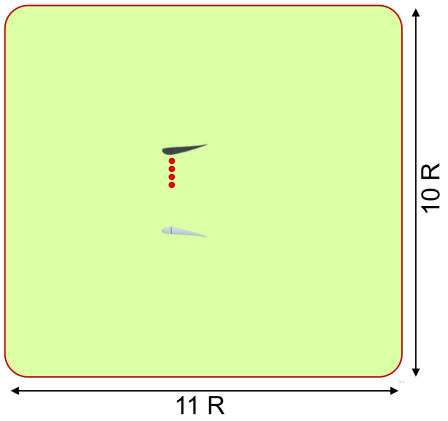

Figure 6: Acoustic FEM domain (green volume), AML (red line) and rotating dipoles (red circles).

2.2.2. Broadband trailing-edge noise

The prediction of the trailing edge broadband noise has been obtained following Amiet (1975, 1976). In this semi-analytical framework based on

Curle's analogy (Curle, 1955), the equivalent source of noise is the unsteady wall pressure field induced by the advection of the turbulent boundary layer past the trailing edge. Both the aerodynamic interaction and acoustic radiation models rest on thin airfoil theory and the application of Schwartzchild's theorem (Roger and Moreau, 2005).

The model provides the following solution for the sound power spectral density at the observer position $\mathbf{x} = (x_1, x_2, x_3)$ and angular frequency ω (with the coordinate axes defined in Fig. 7):

$$S_{pp}(\mathbf{x}, \omega) = \left(\frac{\omega \, x_3 \, c}{4\pi \, c_0 \, \sigma_0^2} \right)^2 \frac{L}{2} \left| \mathcal{L} \left(x_1, \omega/U_c, k\frac{x_2}{\sigma_0} \right) \right|^2 l_y \left(k\frac{x_2}{\sigma_0}, \omega \right) \Phi_{pp}(\omega) \quad (4)$$

where c and L are respectively the chord and span, $\mathcal{L}$ is the aeroacoustic transfer function given in Roger and Moreau (2005), l_y and Φ_{pp} are the spanwise coherence length and the point spectral density, respectively, of the pressure field just upstream of the trailing edge. $\sigma_0 = \sqrt{x_1^2 + \beta^2(x_2^2 + x_3^2)}$ is the distance from the airfoil to the listener corrected by the convection effects with $\beta^2 = 1 - M^2$, with M being the freestream Mach number $M = U/c_0$ based on the speed of sound c_0. Finally, U_c is the convective velocity and k denoting the acoustic wavenumber.

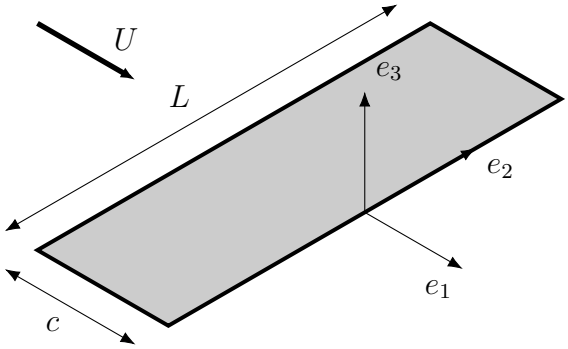

Figure 7: Reference Frame used for trailing-edge noise prediction.

The wall pressure spectrum (WPS) Φ_{pp} has been obtained from different semi-empirical models, having in common the same functional shape

$$\frac{\Phi_{pp}(\omega)}{\Phi^*} = \frac{a(\omega^*)^b}{[i(\omega^*)^c + d]^e + [f R_T^g \, \omega^*]^h} \quad (5)$$

where $\omega^* = \omega \, \delta / U_e$ is the non-dimensional angular frequency defined as a function of the boundary layer thickness δ and freestream velocity U_e.

$\Phi^* = \tau_{wall}^2\,\delta^*/U_e$ is the scaling factor for the spectrum combining inner and outer boundary layer variables: the wall shear stress τ_{wall}, the displacement thickness δ^* and the external velocity U_e. The parameter $R_T = u_\tau^2\,\delta/(U_e\,\nu)$ is acting as a Reynolds number. Slightly modified variants of (5) have been proposed in the literature (Goody, 2004; Rozenberg et al., 2012; Lee and Shum, 2019) to account for the effect of adverse / favorable pressure gradients on the pressure spectrum, through additional parameters such as the Clauser parameter β_C, Coles' wake parameter Π and the shape factor ϕ^*.

The coefficients a, b, ... h in the expression (5) can be tuned to match asymptotic behaviour, manually fit to a database or obtained from multiples databases using machine-learning procedures (Rozenberg et al., 2012; Dominique et al., 2021; Kamruzzaman et al., 2015; Lee, 2018). In any case, the procedure involves the extraction of boundary layer parameters such as U_e, δ, δ^*, τ_{wall}, the momentum thickness θ, the friction velocity u_τ, or the pressure gradient $\mathrm{d}p/\mathrm{d}x$.

In this work, the models proposed by Lee and Kamruzzaman have been used, having been proved more accurate than others in the presence of adverse pressure gradients (APG), such as found on the blade suction side close to the trailing-edge.

Lee and Shum (2019)'s model writes as:

$$\frac{\Phi_{pp}(\omega)U_e}{\tau_{wall}^2\,\delta^*} = \frac{a\,\max(1,(0.25\beta_c - 0.52))\,(\omega^*)^2}{[4.76\,(\omega^*)^{0.75} + d^*]^e + [8.8\,R_T^{-0.57}\,\omega^*]^h} \tag{6}$$

where $\beta_c = (\theta/\tau_{wall})/(dp/dx)$, $\Pi = 0.8(\beta_c + 0.5)^{3/4}$, $\Delta = \delta/\delta^*$. The coefficients a and d^* are calculated as follows:

$$\begin{aligned} a &= 2.82\,\Delta^2(6.13\Delta^{-0.75} + d)^e\,[4.2(\Pi/\Delta) + 1] \\ d &= 4.76(1.4/\Delta)^{0.75} \\ d^* &= d \quad \text{if} \quad \beta_c \geq 0.5 \\ &= \max(1.0, 1.5d) \quad \text{if} \quad \beta_c < 0.5 \end{aligned}$$

where $e = 3.7 + 1.5\beta_c$ and $h = \min(3, (0.0139 + 3.01043\beta_c)) + 7$.

Kamruzzaman et al. (2015)'s model is defined as:

$$\frac{\Phi_{pp}(\omega)U_e}{\tau_{wall}^2\,\delta^*} = \frac{0.45[1.75(\Pi^2\,\beta_c^2)^m + 15]\,(\omega^*)^2}{[(\omega^*)^{1.637} + 0.27]^{2.47} + [1.15\,R_T'^{-0.2857}\,\omega^*]^7} \tag{7}$$

where $R_T' = u_\tau^2\,\delta^*/(U_e\,\nu)$ is the modified timescale ratio, $m = 0.5(H/1.31)^{0.3}$, and $H = \delta^*/\theta$ is the shape factor. The modified Clauser's parameter β_c' is

obtained through an experimental database curve-fit with the expression:

$$\beta_c' = ([(1 - \frac{1}{H}) \sqrt{2/C_f} + 1.7] / 6.1)^2 - 1.81 \tag{8}$$

where C_f is the friction coefficient and finally Cole's wake parameter Π is obtained using the same expression as in Lee's model, except for $\beta_c \leq -0.5$ where $\Pi = 0.227$.

To account for the variations of the blade geometry and flow properties along the blade span, Amiet's model is applied following a blade strip approach. The identification of the boundary layer parameters, the calculation of the wall pressure spectra are thus performed for each strip independently. But in contrast with the tonal noise model also based on a blade segmentation approach, the sound contributions of adjacent strips obtained from Amiet's model are decorrelated as the strip widths are assumed to be larger than the spanwise correlation length, so that their emitted noise levels are summed up in terms of power spectral density.

2.3. Flow simulation models

Two low-cost simulation strategies have been implemented for the calculation of the input parameters needed by the noise models described in the previous section. In the first approach, a three-dimensional RANS simulation resolves the boundary layers over the blades and diffuser. In the second case, the induction effect of the diffuser on the blades is calculated with an in-house vortex panel method (VPM), and a strip method based on two-dimensional RANS simulations is used to obtain the boundary layer parameters at different blade spanwise locations.

2.3.1. Three-dimensional RANS simulations of the rotor and diffuser

Incompressible RANS simulations have been performed using Simcenter STAR-CCM+ finite volume solver (Siemens Digital Industries Software, 2022b), over a sector spanning over 120° of azimuthal angle, as visible in Fig. 8. The radial extent of the computational domain is of $13R$, where R is the blade tip radius. Its streamwise extent is of $20R$, centered on the rotor plane.

The $k - \omega$ Shear Stress Transport (SST) turbulence model of Menter (1994) has been used, following established practices from the literature Bontempo et al. (2023); Saleem and Kim (2019); Roshan et al. (2015); Noorollahi et al. (2019); Küçükosman (2019); Knight et al. (2018). A Moving Reference

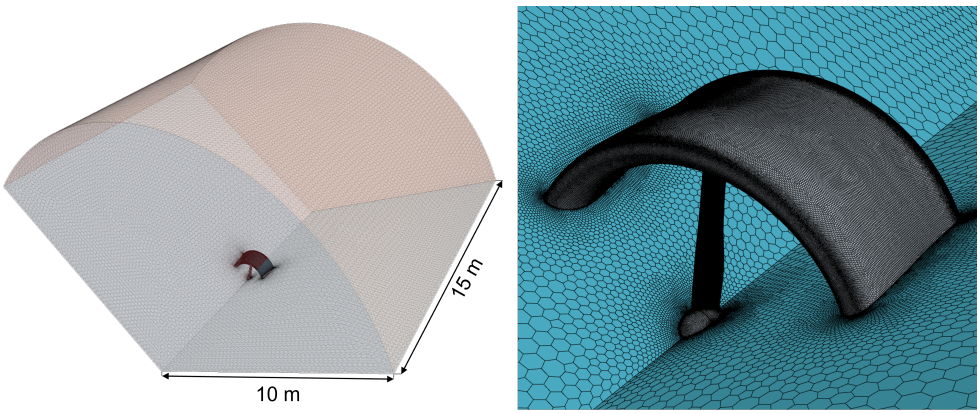

Figure 8: CFD domain and Fine mesh in Simcenter STAR-CCM+ software.

Frame (MRF) approach was used to model the rotation of the turbine blades. The rotating domain includes the blades and hub, the wall of the diffuser being static. No-slip boundary conditions are prescribed to all solid surfaces. The freestream wind velocity U_∞ was imposed at the domain inlet, periodic boundary conditions at the sides of the azimuthal sector, and pressure outlet boundary conditions at the remaining external boundaries.

The 3D domain was discretized using a polyhedral mesh. A grid sensitivity study has been performed considering five meshes progressively refined at the surface of the duct. The mesh parameters are given in Tab. 2. Fine mesh resolves the boundary layer close to the trailing edges of the blade and diffuser with $y^+ < 1$. The four other grids adopt a coarser resolution at the blade and diffuser surfaces. The number of cells varies from 11.2M cells for Coarse grid up to 31.5M cells for Fine grid.

2.3.2. Vortex Panel Method and Two-dimensional strip approach

Assuming radial equilibrium, the flow field over each blade section can be approximated using a two-dimensional approach. The blade geometry is cut at successive radii, generating an airfoil at each radius r subjected to an incoming flow vector $\mathbf{U}_{2D}(r)$, that is the resultant of the axial velocity at the rotor plane and the local tangential velocity:

$$\mathbf{U}_{2D}(r) = U_{\text{panel}}(r)\,\mathbf{e}_x + (\Omega\, r)\,\mathbf{e}_\theta \tag{9}$$

where U_{panel} has been obtained using an in-house code implementing the axisymmetric vortex panel method (VPM) and momentum theory presented

in Lewis (1991); Bontempo and Manna (2020).

In contrast with the classical Blade Element Momentum Theory used for free rotors, this approach accounts for the induction effect of the diffuser and the actuator disk's effect. The VPM code discretizes the diffuser geometry into a pre-selected number of small panels, and places a point vortex at the center of each panel. The strengths of the bound vortices are determined by imposing a zero normal component of the velocity at each panel. Similarly, the zero-thickness wake sheet is segmented into panels and assigned a vorticity that imposes the rotor load by creating a velocity gradient that separate the high-speed external flow from the low-velocity wake region (Bontempo and Manna, 2022). Once the strengths of the point vortices are established, velocity is then calculated using the Biot-Savart law, applied to these vortices, and the induced velocity v at a given location can be calculated accounting for all the panels using:

$$v = \frac{\gamma_n}{2\pi L} \tag{10}$$

where γ_n represents the point vorticity of panel n, and L the distance to the location, measured from the panel's center. As a consequence, when the distance to the wall is smaller than the panel length, the model performs sub-optimally and may lead to inaccurate flow predictions. The velocity U_{panel} is obtained with the same Bio-Savart integration, at any point along the blade radius. The duct was discretized into 200 panels with increased density near the leading and trailing edges to accurately capture areas of higher panel vorticity. This configuration was found to produce converged results of individual point vorticity and far wake radius. Even though VPM is a fast and cheap method, given the duct geometry was defined with 200 points, over-refining beyond this count offers minimal accuracy gains. In this VPM model, the hub is not modelled.

The incoming velocity $\mathbf{U}_{\text{2D}}(r)$ is then used to define the velocity inlet condition of the two-dimensional RANS calculation carried out for each blade strip radius. As for the 3D RANS simulation, the simulations are performed using the $k-\omega$ SST (Menter, 1994) model. An example of 2D computational domain is shown in Fig. 9, with its dimensions provided in terms of chord lengths c. As for the 3D RANS simulations, the blade surface is modeled as a no-slip wall and a pressure outlet condition is used at the external boundary downstream.

The 2D RANS simulation meshes are created following the automated

procedure and best practices proposed by Bresciani et al. (2022). Trimmed meshes containing about 70,000 cells are thus produced, with cell sizes over the airfoil surface about 0.4 mm, going down to 0.03 mm close to the trailing edge. A total of 40 prism layers was used, with a targeted y^+ of 0.4.

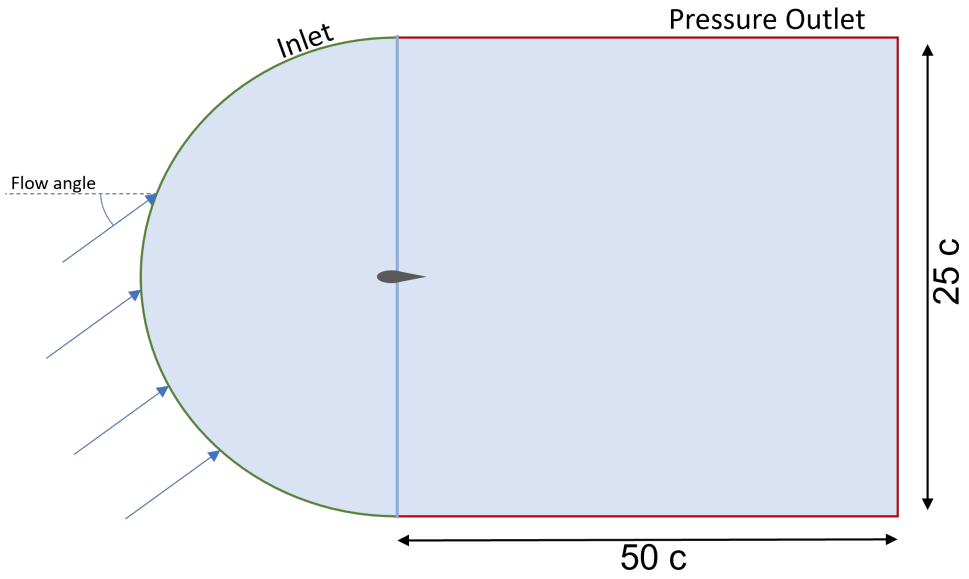

Figure 9: 2D RANS flow domain and boundary conditions used for the strip approach.

3. Application to DonQi turbine

The results obtained for the DonQi turbine at each step of the sound prediction chain (Fig. 4) are presented below.

3.1. Aerodynamic results

Table 2 showcases the evolution of thrust and torque coefficients C_T and C_Q as well as BL layer thickness at suction side for the five different meshes used for 3D RANS simulations.

Table 2: Grid independence study for the 3D CFD setup of the DAWT.

Grid	Cell	y^+		C_T	C_Q	Blade SS BL
	Number	Duct	Blade			δ at $r = 0.69$
Coarse	11.2M	< 50	< 2	0.887	4.89e-2	3.44e-03 m
Medium	15.8M	< 25	< 1.5	0.886	4.89e-2	3.32e-03 m
Medium Fine 1	17.9M	< 18	< 2.5	0.859	4.53e-2	3.46e-03 m
Medium Fine 2	20.1M	< 12	< 2.5	0.853	4.46e-2	3.36e-03 m
Fine	31.5M	< 1	< 1	0.846	4.47e-2	3.30e-03 m

The results tabulated indicate that as y^+ decreases on the blade surface, the boundary layer (BL) thickness and load coefficients tend to converged results. The duct flow resolution is also improved with the duct surface y^+ below 1, achieving a relative difference below 1% (with respect to the Fine mesh) observed in the torque coefficient (C_Q) and thrust coefficient (C_T) between the two finest meshes. The BL thickness on the blade trailing edge shows higher uncertainty, yet the relative difference is less than 5% even for the coarse mesh.

The Fine grid's low relative difference (compared to the previous grids) demonstrates the 31.5 million cells is fine enough for the present work. Furthermore, the thrust coefficient C_T of the Fine grid shows a discrepancy below 2%, compared to the benchmark LBM result presented in Table 1.

3.1.1. Aerodynamic modeling validation

Figure 10 shows the velocity contour plots obtained on the meridional plane using three-dimensional RANS and the axisymmetric VPM code. Both methods provide a similar prediction of the acceleration, being the strongest close to the diffuser throat, and of the same wake width downstream of the diffuser.

However, the simplified approach, by omitting viscous effects, results in abrupt transition across the wake vorticity film, opposed to the distinct velocity gradient between the interior and exterior of the wake observed in the 3D simulation. Additionally, the absence of the hub modelling in the VPM results in axial velocity errors close to the rotor plane, as seen in Fig. 10.

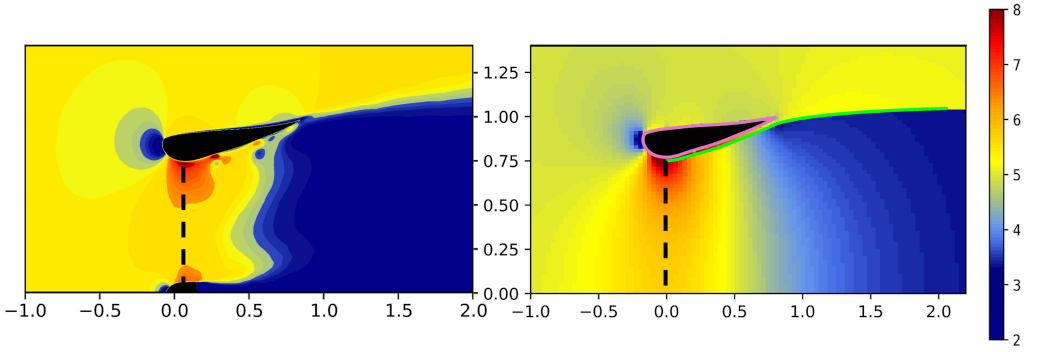

Figure 10: Velocity magnitude (m/s) contour on DAWT middle section from: (left) 3D RANS and (right) VPM with wake (green line).

Figure 11 presents the axial velocity U_∞ along the radius on the rotor plane, obtained in Avallone et al. (2020) using LBM and 2D RANS, compared with our 3D RANS and VPM results. A good match is observed between the 3D RANS results and the reference data for $r > 0.8R_0$. However, the 3D RANS velocity profile reveals a strong influence of the hub, close to $r/R_0 = 0.2$, which is not corroborated by the LBM results; the VPM overpredicts the velocity by about 10% in the tip region. The discrepancy is more pronounced close to the hub, which is not modelled by the VPM simulation.

The VPM is expected to overestimate the angle of attack used for the two-dimensional strip approach, due to its dependence on $U_{\text{panel}}(r)$. However, as the rotational component $\Omega\, r$ outweighs $U_{\text{panel}}(r)$ at the tip, the error impact is estimated to diminish at this position.

Figure 12 presents VPM outputs used as input for the two-dimensional strip approach, including the angle of attack (AoA) and the velocity magnitude U_{mag}, later used as $\mathbf{U}_{\text{2D}}(r)$ as schematized in Fig. 4. The figure compares the VPM results with other methodologies. The intermittent black lines in the figure indicate the locations of the three blade sections (tip, middle, and root) that represent the overall behavior of the turbine.

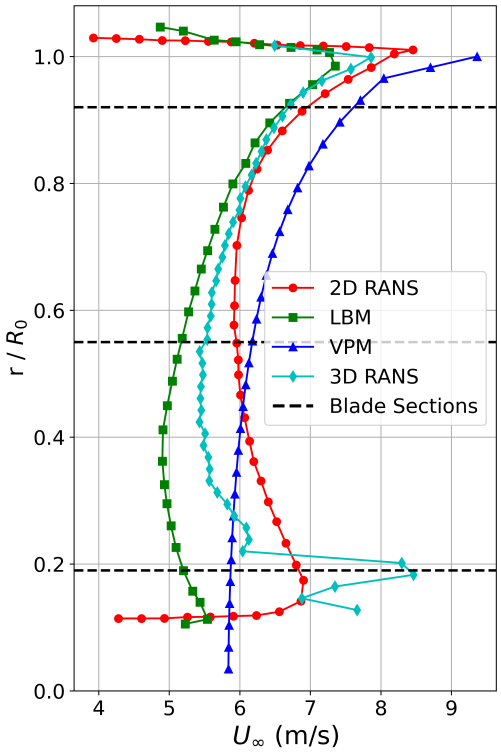

Figure 11: Axial velocity distribution on the rotor plane from 3D RANS and VPM. Present results are compared with LBM (Avallone et al., 2020) and 2D RANS (Dighe et al., 2019) results from the literature.

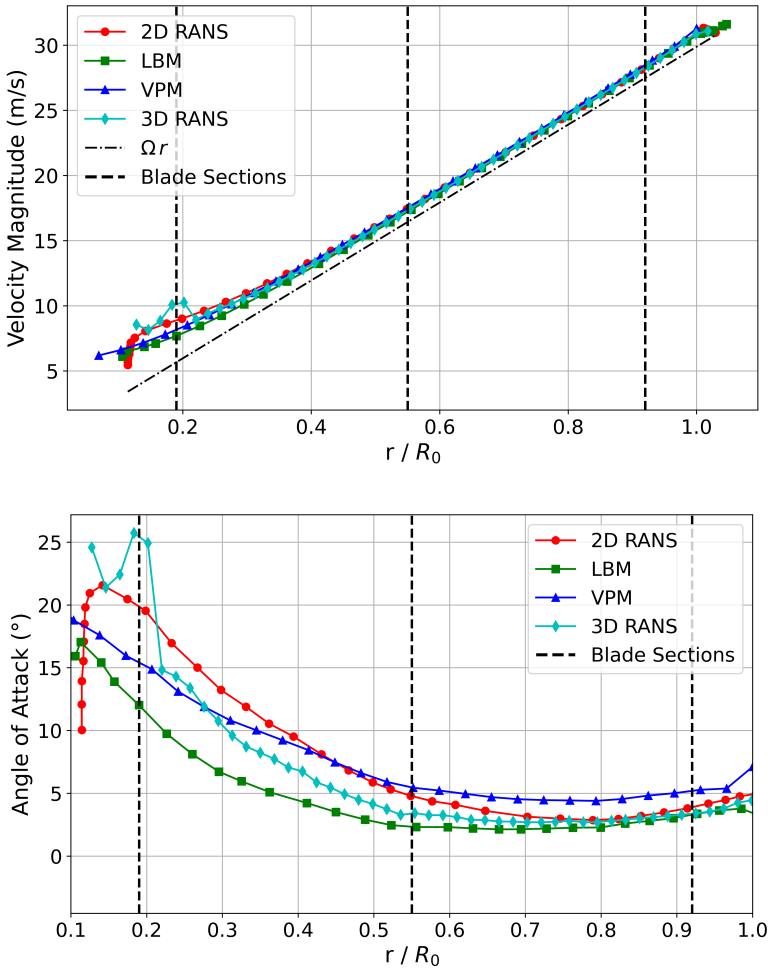

Figure 12: Two-dimensional strip approach inputs from VPM, compared with methods of higher fidelity (top) Velocity Magnitude and (bottom) Angle of Attack, compared with LBM (Avallone et al., 2020) and 2D RANS (Dighe et al., 2019).

The VPM velocity magnitude aligns closely with other methods across the entire span of the blade. As for the angle of attack, the VPM's estimation shows consistent overprediction of 2 to 5° with respect to the LBM results. The overestimation diminishes towards the blade tip, resulting of the rotational component's increased weight on the angle of attack. The 3D RANS shows a significant overprediction of the angle of attack close to Section 1, attributable to the peak in velocity observed in Figure 11. For $r > 0.5R_0$, the angle of attack predictions indicate a consistent alignment with LBM,

with deviations under 2°.

Figure 13 presents the azimuthally averaged C_p distribution on the diffuser, obtained from 3D RANS and VPM. The values were computed using the $5\,\mathrm{m\,s^{-1}}$ wind speed as reference. While there is agreement between the 3D RANS and the VPM results at the duct pressure side, the VPM's C_p prediction is affected by the proximity to the rotor region, deviating on the C_p magnitude in the inner duct.

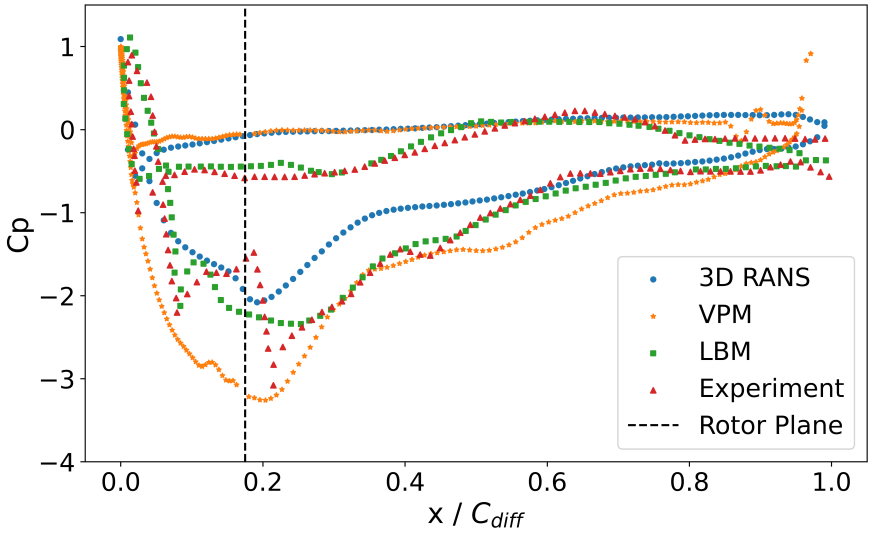

Figure 13: Pressure coefficient along the diffuser chord, compared with LBM and Experiment from reference(Avallone et al., 2020).

The pressure coefficient results obtained in this study are also compared with time-averaged LBM and experimental data of Avallone et al. (2020) in Fig. 13. Comparing the azimuthally averaged C_p with time-averaged LBM results reveals discrepancies from variance in averaging methods.

On the surface of the blades, the C_p profile was compared with Küçükosman (2019) 3D RANS results at 3 sections (x/R = 0.19 , x/R = 0.55 and x/R = 0.92). The comparison is presented in Fig. 14. The plotted pressure coefficients were computed using U_{mag} velocity as the reference value for each section, as detailed in Table 3. The results showcase consistency of the C_p results across the blade's span and chord for both the 3D and VPM + 2D strip approaches.

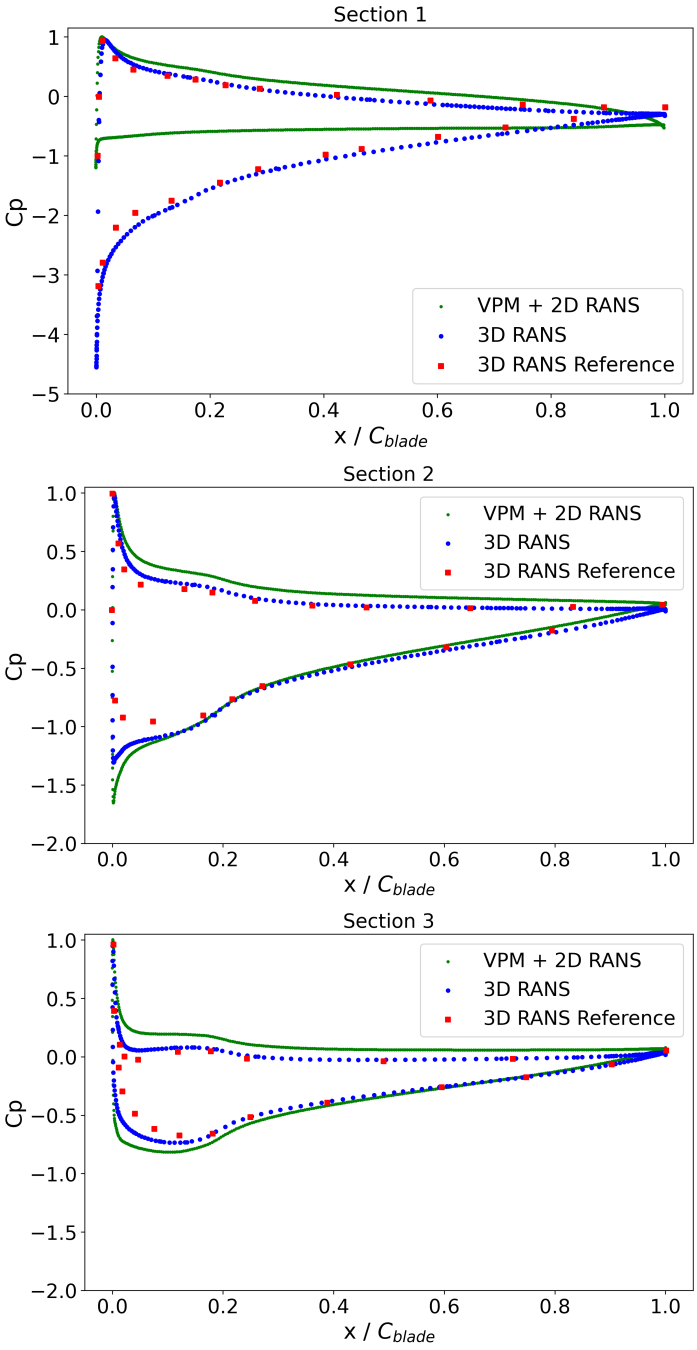

Figure 14: Comparison of $\boldsymbol{C_p}$ on the blade surface with 3D RANS Reference from Küçükosman (2019) at three different radii: Section 1) $\boldsymbol{x/c = 0.19}$; Section 2) $\boldsymbol{x/c = 0.55}$; Section 3) $\boldsymbol{x/c = 0.92}$.

Table 3: Blade sections position and chord, U_{mag} velocities and VPM outputs.

Section #	Radius (m)	Chord (m)	$U_{mag}(m/s)$	VPM $U_{mag}(m/s)$	VPM AoA (°)
1	0.143	0.13	7.56	8.05	35.1
2	0.413	0.12	17.16	17.45	9.7
3	0.690	0.105	27.90	28.17	2.9

For the Sections 2 and 3, the C_p exhibits similar trend when comparing the 3D and VPM + 2D approaches, with relative differences below 5%. The 3D RANS was effective in all blade locations. In Section 1, flow separation is observed for the VPM + 2D RANS method, verified by a mismatch in the C_p. The flow separation results from overprediction of angle of attack or U_{mag} by the VPM. However, as it will be discussed later, due to its higher velocity, the tip region plays a more influential role in terms of noise emission.

3.1.2. Aerodynamic data for noise computation

Boundary layer parameters extracted from the 3D RANS and the 2D strip simulations are compared against the 3D RANS results of Küçükosman (2019) in Fig. 15. Results are shown for blade sections 1, 2 and 3. Due to the flow separation verified in Section 1 with the VPM + 2D RANS approach (Fig. 14), the tip region BL parameters from this methodology were excluded from this analysis.

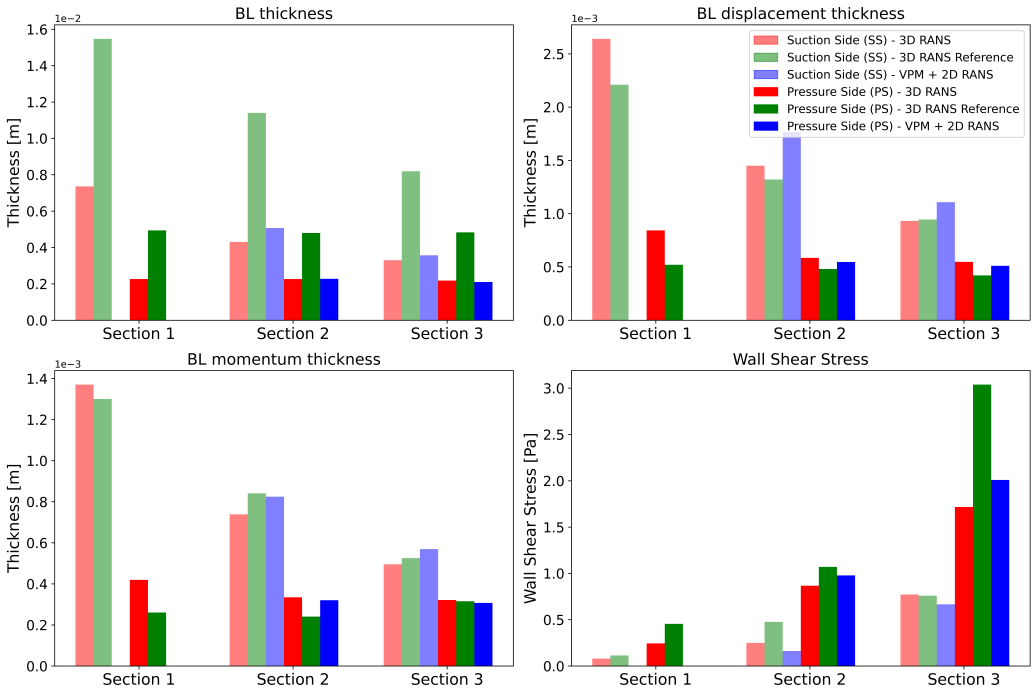

Figure 15: Boundary layer parameters extracted from 3D RANS and 2D strip approach, for 3 sections (PS and SS), compared with Küçükosman (2019) 3D RANS.

The 3D RANS and VPM + 2D RANS methodologies are in agreement across all sections and parameters. Regarding the BL thickness, both methodologies yield lower value than Küçükosman's 3D RANS results. Discrepancies may be attributed to the usage of different methods for determining BL thickness. More specifically, in this study, the BL thickness was calculated using a mean-vorticity based method for its higher accuracy (Griffin et al., 2021), relative to the total pressure approach used by Küçükosman.

Since both the momentum thickness and the displacement thickness are integral quantities, resulting in 3D RANS and VPM + 2D RANS predictions having improved agreement to Küçükosman's results. Still, as detailed in Fig. 15, non negligible differences are observed between the VPM + 2D and 3D RANS BL parameters, especially for Section 2. The agreement is better at Section 3, with relative differences ranging between 4% and 17% for the momentum thickness and the wall shear stress, respectively.

These extracted blade boundary layer parameters are used as inputs of the Lee and Kamruzzaman models, and the resulting wall pressure spectra

are plotted in Figs. 16, 17 and 18 for the three sections using the 3D and 2D strip methods.

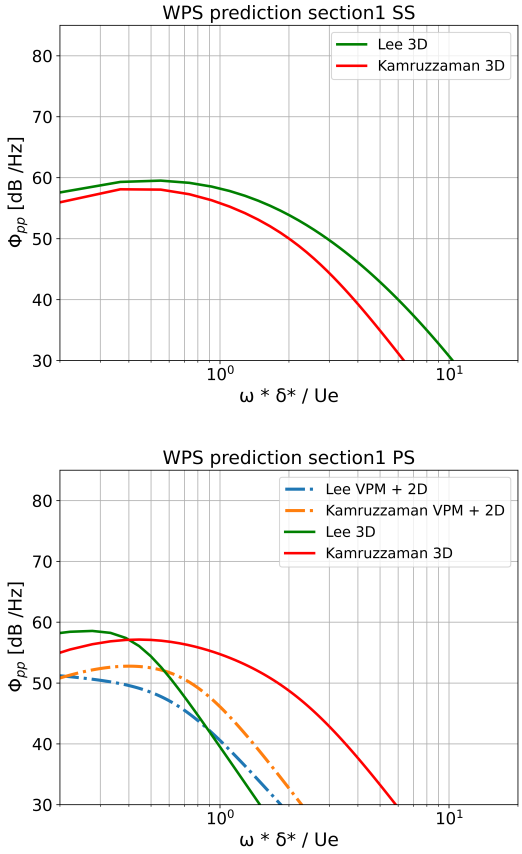

Figure 16: Wall pressure spectrum predictions using different WPS models, for Section 1: Suction Side (left) and Pressure Side (right).

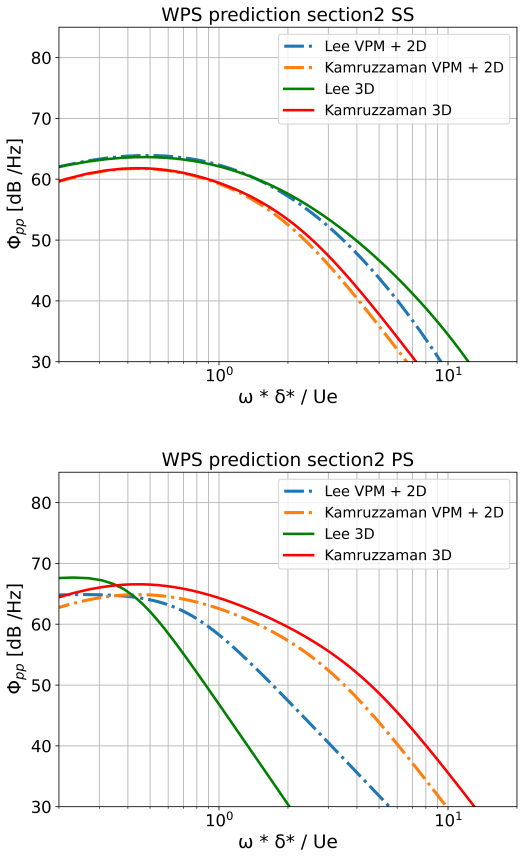

Figure 17: Wall pressure spectrum predictions using different WPS models, for Section 2: Suction Side (left) and Pressure Side (right).

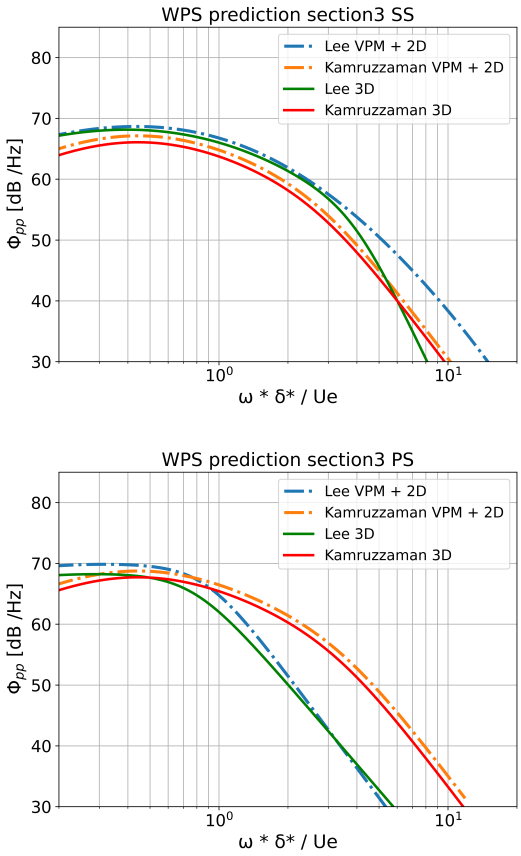

Figure 18: Wall pressure spectrum predictions using different WPS models, for Section 3: Suction Side (left) and Pressure Side (right).

The wall pressure spectra ϕ_{pp} obtained for the various blade sections yielded increasing magnitude closer to the tip. The spectra at the suction side reveal greater match by both models and methods. On the other hand, the pressure side's challenging conditions lead to a poor agreement between the models, particularly in sections 1 and 2. Despite this, the maximum magnitudes of the spectrum across the models are consistent.

3.2. Aeroacoustic results

The DonQi rotor noise prediction is computed according to the methodology of Fig. 4 and the results are presented below, considering both broadband and tonal noise components.

3.2.1. Free-field Rotor Broadband Noise

Figure 19 presents of the acoustic pressure at 10 m downstream of the rotor axis for both the 3D and VPM + 2D RANS strip approaches. The acoustic spectra are also provided for each individual strip, demonstrating their noise relative noise contribution across the frequency spectrum for each blade region and computational approach. The blade tip segment contributes the most, essentially defining the total acoustic TE noise emission of the full blade. Conversely, the strip closest to the root has a negligible contribution. This one is also the only strip for which the 2D and 3D approaches give significantly different results. This is consistent with the differences observed above regarding the flow characteristics, due in particular to the absence of flow deflection by the hub in the 2D calculations.

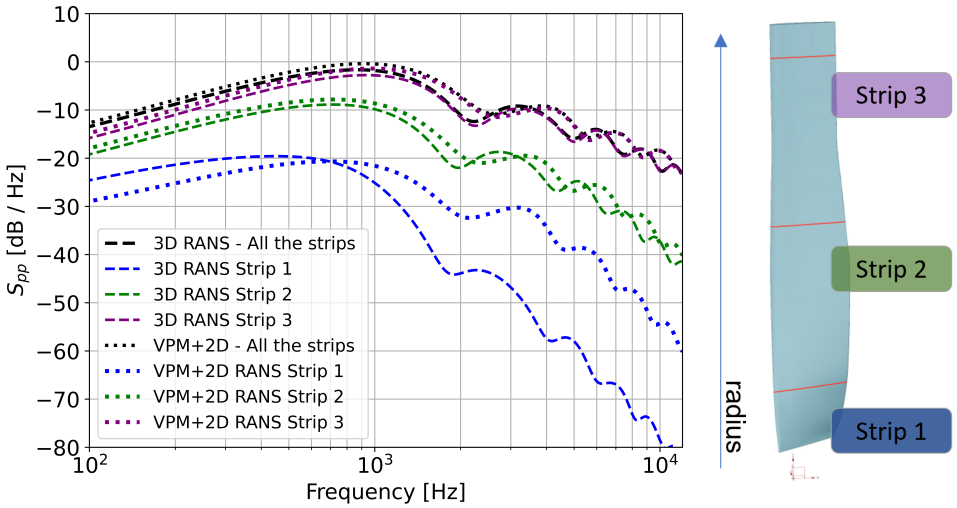

Figure 19: Rotor PSD at 10 m distance, downstream of the rotor axis under free-field conditions. Separate and total contribution from the 3 different strips, for the 3D RANS and VPM+2D RANS.

The segment independence study, available in Appendix A, determined that the blade's outermost 35 % was the key contributing region for TE noise. Furthermore it was shown that discretizing this region with three strips is sufficient to provide a reliable prediction of the maximum S_{pp} magnitude.

The rotor broadband TE noise free-field predictions obtained using Amiet's

model (4) with both the 3D and 2D RANS strip approaches to compute the Lee and Kamruzzaman wall pressure spectra, are shown in Figs. 20, 21 and 22 at three microphone positions. The microphones, located at 30°, 90° and 120° relative to the upstream direction, sit at a 3 m distance ($4\,r$) from the rotor origin. The present results are compared to the far-field high-fidelity LBM+FW-H predictions from Avallone et al. (2020). The LBM simulation is carried out including both the rotor and the diffuser. The sound predictions at the microphones are then obtained by FW-H technique. Only LBM+FW-H results obtained using the rotor as impermeable FW-H surface are reported. In that way, both the present Amiet's TE noise predictions and the LBM results from Avallone et al. (2020) assume free-field propagation from the rotor blades. The cut-off frequency of the LBM spectra is expected to be of 4 kHz (Avallone et al., 2020). It is also important to note that since the rotor BPF is of 19 Hz, at frequencies above 200 Hz the noise tonal component is expected to be negligible, so Figs. 20, 21 and 22 show only broadband noise. The peak levels and frequencies are in fair agreement. It is also visible that the difference between the sound predictions obtained from the Lee and Kamruzzaman models is of the same order of magnitude as observed in the wall pressure spectra.

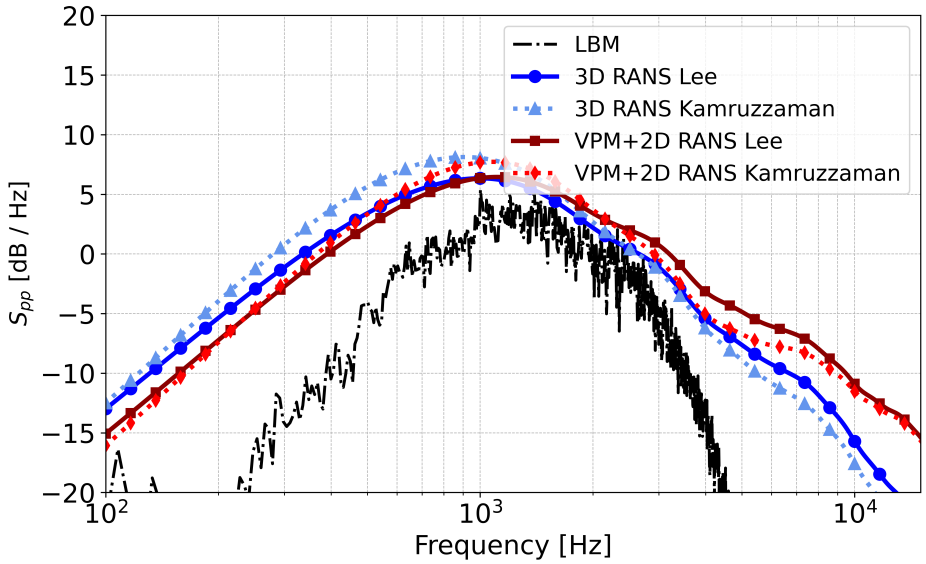

Figure 20: Rotor trailing edge broadband noise PSD prediction at 3 m from the rotor origin and 30° relative to the upstream direction.

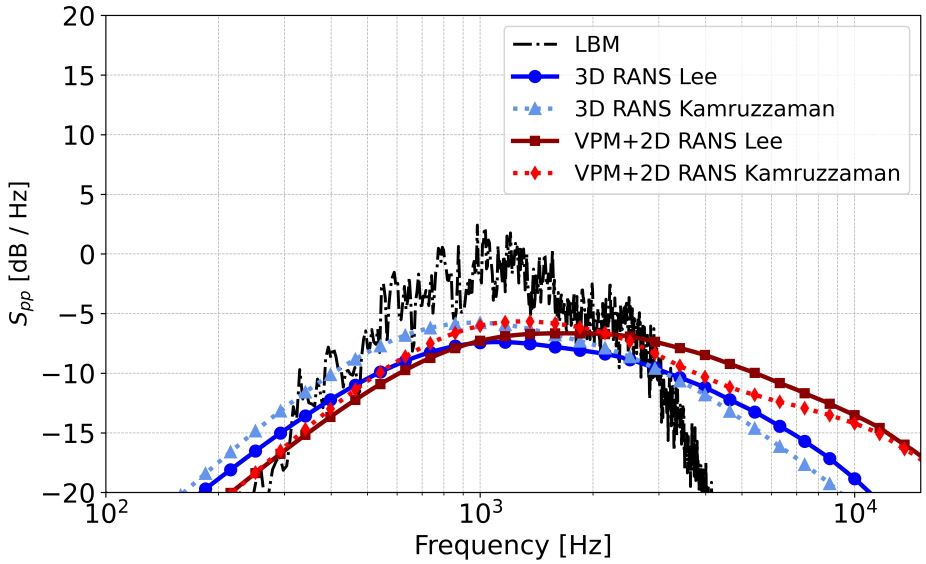

Figure 21: Rotor trailing edge broadband noise PSD prediction at 3 m from the rotor origin and 90° relative to the upstream direction.

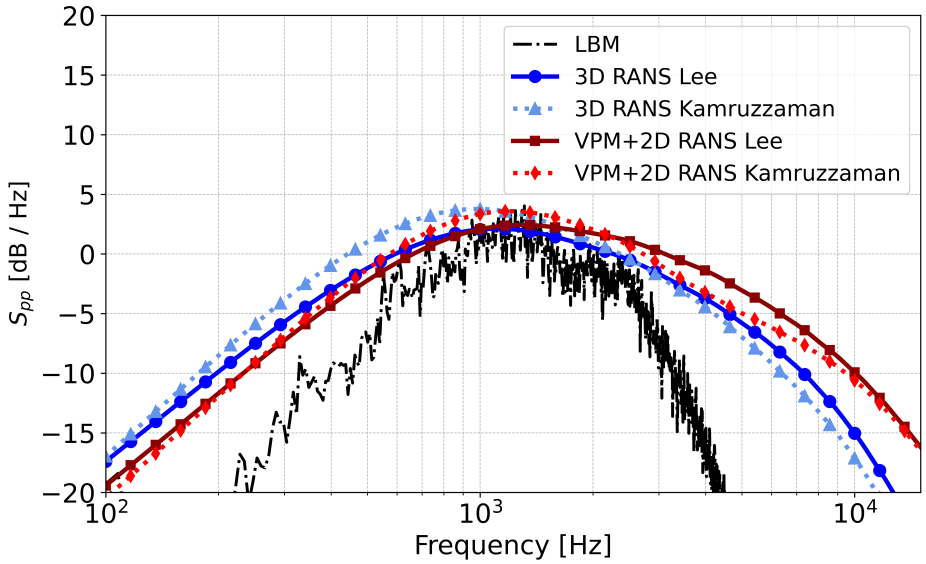

Figure 22: Rotor trailing edge broadband noise PSD prediction at 3 m from the rotor origin and 120° relative to the upstream direction.

The best agreement between the 3D-RANS / VPM-2D-RANS approaches and the reference LBM results is obtained at the polar angle 120°, where the peak values around 1 kHz are comparing quite well. The Amiet-based levels exceed the LBM ones away from the main peak, especially at high frequencies, but the spectral shape remains reasonably well predicted considering the differences of computational effort, falling within a 5 dB accuracy. Despite this, the present method fails to capture the low and high frequency decays. The reasons for this discrepancy remain unclear.

3.2.2. Tonal Noise and Scattering effect of diffuser

The tonal steady loading noise emitted by the rotor and scattered by the diffuser has been predicted using the metholodogy described in 2.2.1. The blade forces, calculated from the integration of the steady pressure obtained in the 3D CFD simulation were used as input for the tonal noise predictions. The FEMAO simulations in Simcenter 3D were conducted using a 50 mm element size tetrahedral mesh, and 15 AML layers, both design to ensure mesh and AML independent results. The frequencies of interest were the ten first multiples of the Blade Passing Frequency (BPF), ranging from 19 to 190 Hz. For a frequency of 500 Hz and a conservative value of $N_s = 10$ results

in a segment length $L_s = 0.068\,\mathrm{m}$, amounting to around 11 segments for the 0.75 m DonQi blade, as calculated using Equation (2).

Very low sound levels were obtained at BPF harmonics. Their contribution is therefore considered insignificant for the scope of this analysis. In the following, acoustic results are therefore only presented at the BPF.

Figure 23 (left) presents the tonal directivity of the DonQi rotor at the BPF in free-field conditions, at a distance of 3 m surrounding the rotor. The results obtained using the FEMAO results, and compared to the solution calculated using the analytical near-field formulation (3) for loading noise. Comparison with LBM is challenging and not shown here due to the short simulated physical time in LBM, resulting in a frequency resolution for the acoustic spectra which is too low for analysing the tonal pressure at the BPF. The directivity plot showcases a symmetry with respect to the rotor plane. The agreement between the numerical results and the analytical solution is excellent, thereby validating the FEMAO sound propagation approach for a free field configuration.

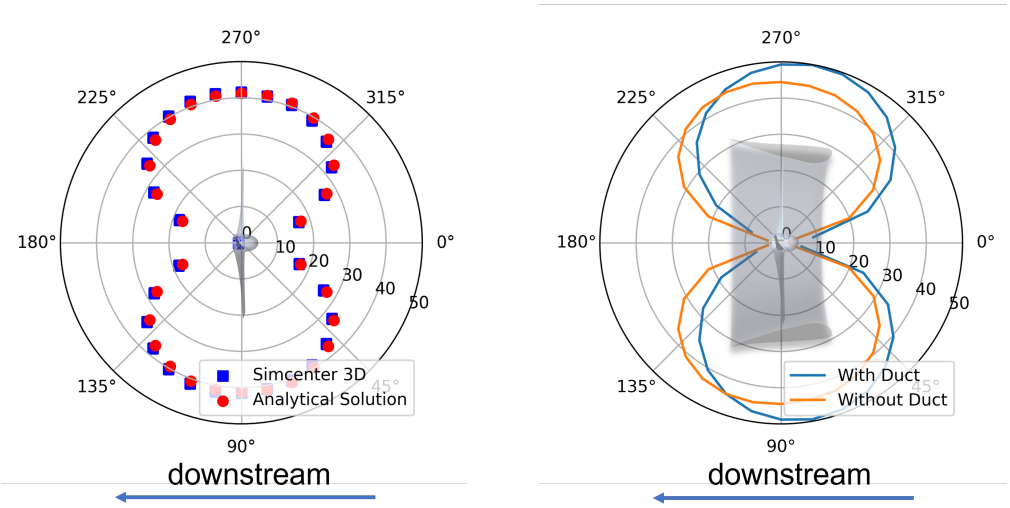

Figure 23: Tonal noise directivity plots at the BPF in dB at 3 m: FEMAO results against analytical solution for unducted rotor (left) and FEMAO results for ducted and free-field rotors (right).

Building upon these findings, Fig. 23 (right) presents the directivity of the steady loading tonal noise at the BPF in both an open and ducted configuration, using the DonQi diffuser. The results show the scattering effects

by the diffuser, which amplifies the tonal pressure peak and shifts the peak values towards the upstream direction, breaking the symmetry observed in free-field. Maximum differences of about 8 dB are reported between the ducted and free-field rotors at 3 m.

4. Conclusions

In this study, a numerical approach has been proposed to predict the aerodynamic noise produced by the rotor of a diffuser-augmented wind turbine. The methodology relies on either a 2D or 3D RANS flow simulation. Broadband TE noise predictions are computed with Amiet theory analytical model. Tonal noise predictions accounting for the scattering effect caused by the diffuser are obtained using a hybrid high-order finite element approach in the frequency domain. The methodology was applied to the DonQi wind turbine. The numerical results reveal the present approach leads to a fair prediction of the noise spectrum maximum amplitude and corresponding frequency.This study also revealed that inputs from the lower-fidelity approach (VPM + 2D RANS strip approach) can yield results of comparable accuracy to those obtained with a more computationally intensive method (3D RANS).

It was identified that most broadband trailing-edge noise is localized within the final third of the blade and employing three strips within this region proved sufficient for accurate trailing-edge noise prediction. Regarding the tonal noise, it was noted that the first BPF induces a significant amplitude, accounting only for the steady loading component. Further investigation into the unsteady component and the volume displacement term would be beneficial for a more accurate prediction.

In terms of noise directivity, the diffuser structure plays an evident role in the tonal noise scattering. While in a free-field scenario the loading noise directivity in strongest on the direction of the rotor plane, with the inclusion of the diffuser, a directivity shift with amplification towards the upstream direction is observed, while attenuating it downstream. In contrast, broadband noise manifests a pronounced intensity along the rotor's axis, predominantly downstream.

While we have thoroughly examined the dominant sources of rotor noise, to truly understand the complete acoustic footprint of the DAWT, it is critical to investigate the diffuser self noise. Of particular significance is the noise emanating from the diffuser trailing edge, as preliminary indications suggest

that it may be an important noise source, requiring further consideration in future research.

Appendix A. Trailing edge broadband noise segment independence

The outermost 35% segment of the blade was determined to be the key contributing region for TE noise. The approach VPM + 2D RANS was used on incremental sections of the blade, displayed in Fig. A.24, which were systematically analyzed starting from the blade tip. The segments ranged from 7 % to as much as 55 % of the blade length, and the objective was to identify the TE noise convergence point. The results showed that a section of 27 % provides a reliable estimate, but extending the analysis to 35 % of the blade from the tip resulted in acceptable convergence below 1 dB. This indicates that regions beyond this 35 % mark contribute negligibly to TE noise at the studied downstream distance.

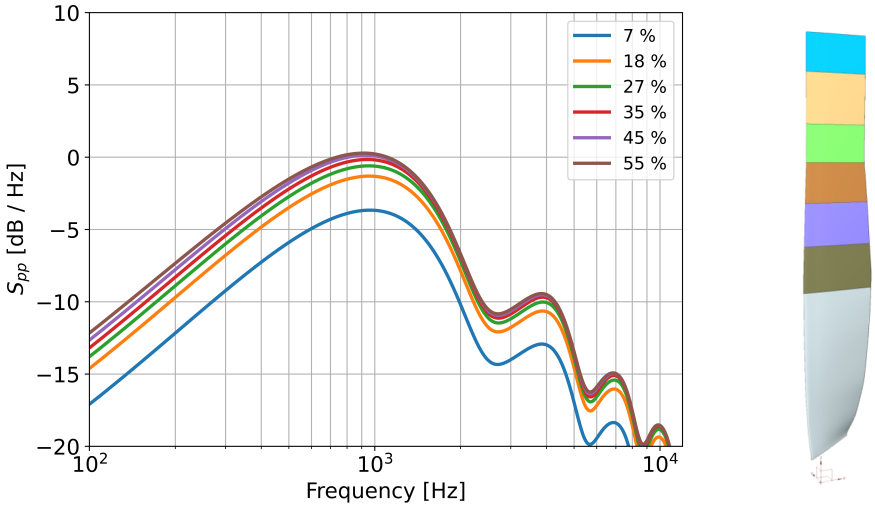

Figure A.24: Rotor Power spectral density at 10 m downstream distance on the rotor axis: analysis of TE noise based on blade length being tested (percentage) starting from the tip.

Upon identifying the outermost 40 % of the blade are the region responsible for the TE noise emission, Fig. A.25 demonstrates how the noise prediction varies with the increasing number of segments subdividing the sector highlighted in blue. The Fig. A.25 demonstrates that three strips suffice for a prediction of the maximum magnitude, around 1000 Hz, with a sub dB accuracy. However, to achieve convergence for higher frequencies more re-

finement is necessary, with results converging on seven strips for the VPM + 2D RANS approach.

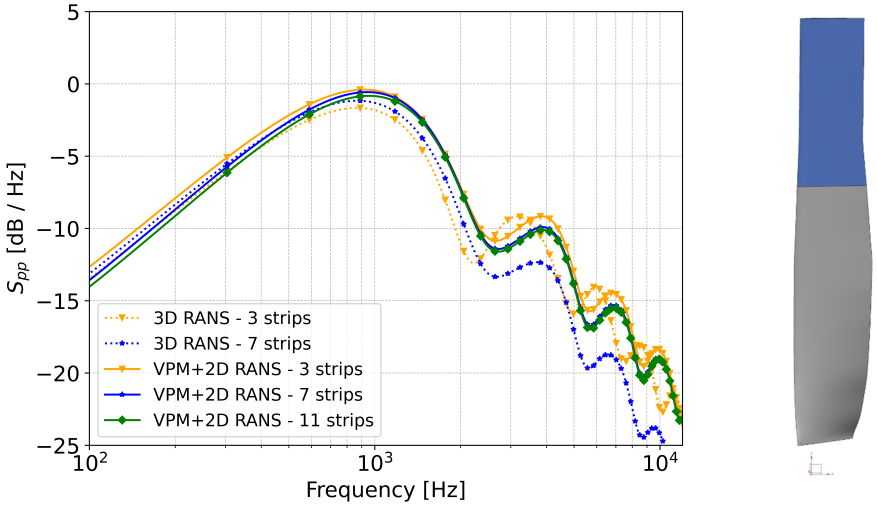

Figure A.25: Influence of varying the number of strips (3, 7, and 11) on the TE broadband noise spectrum for two methods: 3D RANS and VPM+2D RANS.

CRediT authorship contribution statement

Rui Gonçalves: Investigation, Data analysis, Writing - review and editing. **Sophie Le Bras:** Investigation, Data analysis, Writing - review and editing. **Manoel Freire:** Investigation. **Christophe Schram:** Writing - review and editing.

This project has received funding from the European Union's Horizon 2020 research and innovation programme under the Marie Skłodowska-Curie grant agreement No 860101.

References

Amiet, R.K., 1975. Acoustic radiation from an airfoil in a turbulent stream. Journal of Sound and Vibration 41, 407–420. doi:10.1016/S0022-460X(75)80105-2.

Amiet, R.K., 1976. Noise due to turbulent flow past a trailing edge. Journal of Sound and Vibration 47, 387–393. doi:10.1016/0022-460X(76)90948-2.

Anselmi, L., 2017. Computational analysis of ducted wind turbines noise. URL: https://repository.tudelft.nl/islandora/object/uuid%3Afb9c7edd-8011-428e-bd77-f0e80e7bb60f.

Avallone, F., Ragni, D., Casalino, D., 2020. On the effect of the tip-clearance ratio on the aeroacoustics of a diffuser-augmented wind turbine. Renewable Energy 152, 1317–1327. doi:10.1016/J.RENENE.2020.01.064.

Bériot, H., Modave, A., 2021. An automatic perfectly matched layer for acoustic finite element simulations in convex domains of general shape. International Journal for Numerical Methods in Engineering 122, 1239–1261. doi:https://doi.org/10.1002/nme.6560.

Bériot, H., Prinn, A., Gabard, G., 2016. Efficient implementation of high-order finite elements for helmholtz problems. International Journal for Numerical Methods in Engineering 106, 213–240. doi:10.1002/nme.5172.

Bontempo, R., Manna, M., 2017. The axial momentum theory as applied to wind turbines: some exact solutions of the flow through a rotor with radially variable load. Energy Conversion and Management 143, 33–48. doi:10.1016/J.ENCONMAN.2017.02.031.

Bontempo, R., Manna, M., 2020. Diffuser augmented wind turbines: Review and assessment of theoretical models. Applied Energy 280, 115867. doi:10.1016/J.APENERGY.2020.115867.

Bontempo, R., Manna, M., 2022. The joukowsky rotor for diffuser augmented wind turbines: design and analysis. Energy Conversion and Management 252, 114952. doi:10.1016/J.ENCONMAN.2021.114952.

Bontempo, R., Marzo, E.M.D., Manna, M., 2023. Diffuser augmented wind turbines: A critical analysis of the design practice based on the ducting of an existing open rotor. Journal of Wind Engineering and Industrial Aerodynamics 238, 105428. doi:10.1016/J.JWEIA.2023.105428.

Brandetti, L., Avallone, F., Tavernier, D.D., LeBlanc, B., Ferreira, C.S., Casalino, D., 2023. Assessment through high-fidelity simulations of a low-fidelity noise prediction tool for a vertical-axis wind turbine. Journal of Sound and Vibration 547. doi:10.1016/J.JSV.2022.117486.

Bresciani, A.P., Le Bras, S., de Santana, L.D., 2022. Generalization of amiet's theory for small reduced-frequency and nearly-critical gusts. Journal of Sound and Vibration 524, 116742. doi:10.1016/j.jsv.2021.116742.

Brooks, T.F., Pope, D.S., Marcolini, M.A., 1989. Airfoil self-noise and prediction.

Bériot, H., Prinn, A., Gabard, G., 2016. Efficient implementation of high-order finite elements for helmholtz problems. International Journal for Numerical Methods in Engineering 106, 213–240. doi:10.1002/NME.5172.

Cabrol, M., Detandt, Y., Mendonca, F., D'udekem, D., Manera, J., 2012. Computational aeroacoustic analysis of industrial fan application using a hybrid approach, in: FAN2012 Conference, pp. 18–20.

Curle, N., 1955. The influence of solid boundaries upon aerodynamic sound. Proceedings of the Royal Society of London. Series A. Mathematical and Physical Sciences 231, 505–514. doi:10.1098/rspa.1955.0191.

Dighe, V.V., Avallone, F., van Bussel, G., 2020. Effects of yawed inflow on the aerodynamic and aeroacoustic performance of ducted wind turbines. Journal of Wind Engineering and Industrial Aerodynamics 201, 104174. doi:10.1016/J.JWEIA.2020.104174.

Dighe, V.V., de Oliveira, G., Avallone, F., van Bussel, G.J., 2019. Characterization of aerodynamic performance of ducted wind turbines: A numerical study. Wind Energy 22, 1655–1666. doi:10.1002/WE.2388.

Dominique, J., Christophe, J., Schram, C., Sandberg, R.D., 2021. Inferring empirical wall pressure spectral models with gene expression programming. Journal of Sound and Vibration 506, 116162. doi:10.1016/j.jsv.2021.116162.

Ffowcs Williams, J., Hawkings, D., 1969. Sound generation by turbulence and surfaces in arbitrary motion. Philosophical Transactions of the Royal Society of London. Series A, Mathematical and Physical Sciences 264, 321–342. doi:10.1098/rsta.1969.0031.

Gabard, G., Bériot, H., Prinn, A.G., Kucukcoskun, K., 2018. Adaptive, high-order finite-element method for convected acoustics.

https://doi.org/10.2514/1.J057054 56, 3179–3191. doi:10.2514/1.J057054.

Ghasemian, M., Nejat, A., 2015. Aerodynamic noise prediction of a horizontal axis wind turbine using improved delayed detached eddy simulation and acoustic analogy. Energy Conversion and Management 99, 210–220. doi:10.1016/j.enconman.2015.04.011.

Goody, M., 2004. Empirical spectral model of surface pressure fluctuations. AIAA Journal 42, 1788–1794. doi:10.2514/1.9433.

Griffin, K.P., Fu, L., Moin, P., 2021. General method for determining the boundary layer thickness in nonequilibrium flows. Physical Review Fluids 6, 024608. doi:10.1103/PhysRevFluids.6.024608.

Hansen, M.O.L., Sørensen, N.N., Flay, R.G.J., 2000. Effect of placing a diffuser around a wind turbine. Wind Energy 3, 207–213. doi:10.1002/WE.37.

Hanson, D.B., 1980. Helicoidal surface theory for harmonic noise of propellers in the far field. AIAA Journal 18, 1213–1220. doi:10.2514/3.50873.

Hoopen, P.T., 2009. An experimental and computational investigation of a diffuser augmented wind turbine: With an application of vortex generators on the diffuser trailing edge. URL: https://repository.tudelft.nl/islandora/object/uuid%3Af874600f-7cf3-468e-b6e7-fdadc3441077.

Kaltenbacher, M., Hüppe, A., Reppenhagen, A., Zenger, F., Becker, S., 2017. Computational aeroacoustics for rotating systems with application to an axial fan 55, 3831–3838. doi:10.2514/1.J055931.

Kamruzzaman, M., Bekiropoulos, D., Lutz, T., Würz, W., Krämer, E., 2015. A semi-empirical surface pressure spectrum model for airfoil trailing-edge noise prediction. International Journal of Aeroacoustics 14, 833–882. doi:10.1260/1475-472X.14.5-6.833.

Knight, B., Freda, R., Young, Y.L., Maki, K., 2018. Coupling numerical methods and analytical models for ducted turbines to evaluate designs. Journal of Marine Science and Engineering 2018, Vol. 6, Page 43 6, 43. doi:10.3390/JMSE6020043.

Kucukcoskun, K., Kierkegaard, A., 2022. Accuracy and advantages of hybrid solutions compared to direct noise calculations for low-speed fan noise, in: FAN2022 Conference, Universitäts-und Landesbibliothek Darmstadt. doi:10.26083/tuprints-00021708.

Küçükosman, C., 2019. Semi-analytical approaches for the prediction of the noise produced by ducted wind turbines. Ph.D. thesis. Delft University of Technology. doi:10.4233/uuid:b749675c-edb1-4355-ba09-bf46278077d0.

Lanzafame, R., Messina, M., 2010. Horizontal axis wind turbine working at maximum power coefficient continuously. Renewable Energy 35, 301–306. doi:10.1016/j.renene.2009.06.020.

Lee, S., 2018. Empirical wall-pressure spectral modeling for zero and adverse pressure gradient flows. AIAA Journal 56, 1818–1829. doi:10.2514/1.J056528.

Lee, S., Shum, J.G., 2019. Prediction of airfoil trailing-edge noise using empirical wall-pressure spectrum models. AIAA Journal 57, 888–897. doi:10.2514/1.J057787.

Leloudas, S.N., Lygidakis, G.N., Eskantar, A.I., Nikolos, I.K., 2020. A robust methodology for the design optimization of diffuser augmented wind turbine shrouds. Renewable Energy 150, 722–742. doi:10.1016/j.renene.2019.12.098.

Lewis, R.I., 1991. Vortex Element Methods for Fluid Dynamic Analysis of Engineering Systems. Cambridge University Press. doi:10.1017/CBO9780511529542.

Mahmood, D., Javaid, N., Ahmed, G., Khan, S., Monteiro, V., 2021. A review on optimization strategies integrating renewable energy sources focusing uncertainty factor – paving path to eco-friendly smart cities. Sustainable Computing: Informatics and Systems 30, 100559. doi:10.1016/j.suscom.2021.100559.

Menter, F.R., 1994. Two-equation eddy-viscosity turbulence models for engineering applications. AIAA Journal 32, 1598–1605. doi:10.2514/3.12149.

Noorollahi, Y., Ghanbari, S., Tahani, M., 2019. Numerical analysis of a small ducted wind turbine for performance improvement 39, 290–307. doi:10.1080/14786451.2019.1685520.

Oerlemans, S., Schepers, J.G., 2009. Prediction of wind turbine noise and validation against experiment. International Journal of Aeroacoustics 8, 555–584. doi:10.1260/147547209789141489.

Piellard, M., Bailly, C., 2008. Validation of a hybrid caa method. application to the case of a ducted diaphragm at low mach number. 14th AIAA/CEAS Aeroacoustics Conference (29th AIAA Aeroacoustics Conference) doi:10.2514/6.2008-2873.

Roger, M., 2007. Near-field fan noise modeling an installation effects due to scattering surfaces, Lyon, France.

Roger, M., 2019. Aeroacoustics of installed propellers. Number 2019-02 in von Karman Institute Lecture Series, von Karman Institute for Fluid Dynamics.

Roger, M., Moreau, S., 2005. Back-scattering correction and further extensions of amiet's trailing-edge noise model. part 1: theory. Journal of Sound and vibration 286, 477–506. doi:10.1016/j.jsv.2004.10.054.

Roshan, S.Z., Alimirzazadeh, S., Rad, M., 2015. Rans simulations of the stepped duct effect on the performance of ducted wind turbine. Journal of Wind Engineering and Industrial Aerodynamics 145, 270–279. doi:10.1016/j.jweia.2015.07.010.

Rozenberg, Y., Robert, G., Moreau, S., 2012. Wall-pressure spectral model including the adverse pressure gradient effects. AIAA Journal 50, 2168–2179. doi:10.2514/1.J051500.

Saleem, A., Kim, M.H., 2019. Effect of rotor tip clearance on the aerodynamic performance of an aerofoil-based ducted wind turbine. Energy Conversion and Management 201, 112186. doi:10.1016/J.ENCONMAN.2019.112186.

Siemens Digital Industries Software, 2022a. Simcenter Nastran Acoustics User Guide (version 2022.1).

Siemens Digital Industries Software, 2022b. Simcenter STAR-CCM+ User Guide (version 2210), Siemens.

Van, F.A., Eng, D.B., 2011. An improved rotor design for a diffuser augmented wind turbine: Improvement of the donqi urban windmill. URL: https://repository.tudelft.nl/islandora/object/uuid%3Ac58191fd-dad9-4aa7-8492-113c3b19b7fa.

Weber, J., Becker, S., Scheit, C., Grabinger, J., Kaltenbacher, M., 2015. Aeroacoustics of darrieus wind turbine. International Journal of Aeroacoustics 14, 883–902. doi:10.1260/1475-472X.14.5-6.883.

Zhu, W.J., Shen, W.Z., Barlas, E., Bertagnolio, F., Sørensen, J.N., 2018. Wind turbine noise generation and propagation modeling at dtu wind energy: A review. Renewable and Sustainable Energy Reviews 88, 133–150. doi:10.1016/j.rser.2018.02.029.